Elastic full-waveform inversion for tilted orthorhombic media using lithologic constraints

Ashish Kumar & Ilya Tsvankin
Center for Wave Phenomena and Dept. of Geophysics, Colorado School of Mines, Golden CO 80401
email: akumar1@mines.edu

ABSTRACT
Full-waveform inversion (FWI) is capable of estimating the elastic properties of subsurface rocks including hydrocarbon reservoirs with high spatial resolution. Orthorhombic models are needed to adequately describe typical fractured reservoirs and formations under nonhydrostatic stress. Most existing applications of FWI to orthorhombic media, however, are limited to models with a horizontal symmetry plane. Here, we develop an elastic FWI algorithm for tilted orthorhombic media (i.e., models with tilted symmetry planes) which are typical, for example, for subsalt exploration in the Gulf of Mexico. We assume one of the symmetry planes to coincide with the underlying reflector so that the orientation of that plane can be estimated from migrated images. Orthorhombic models are described using nine velocity-based parameters: the P-wave ($\mathrm{V_{P0}, V_{P1}, V_{P2}}$) and the S-wave ($\mathrm{V_{S0}, V_{S1}, V_{S2}}$) velocities along the symmetry directions and the P-wave symmetry-plane normal-moveout velocities ($\mathrm{V_{nmo,1}, V_{nmo,2}, V_{nmo,3}}$). To reduce nonuniqueness, FWI is constrained using lithologic information, such as the vertical P- and S-wave velocities and density obtained from well logs. A convolutional neural network (CNN) trained on the available well logs is used to predict the facies distribution from sparse borehole information. The developed algorithm is successfully tested on synthetic 3D wide-azimuth multicomponent reflection data. In particular, FWI is applied to an orthorhombic version of the structurally complex 3D SEG-EAGE overthrust model. The obtained high-resolution parameter fields confirm that our FWI algorithm is capable of estimating the essential reservoir attributes from multicomponent surface data and improving migrated images of orthorhombic formations.

Key words: Elastic full-waveform inversion, anisotropy, orthorhombic medium, lithologic constraints, convolutional neural networks

1 INTRODUCTION

Elastic full-waveform inversion (FWI) has the potential to estimate high-resolution elastic parameters from seismic data (Tarantola, 1984; Xu et al., 2012; Brossier et al., 2015; Singh et al., 2021a). In order to adequately evaluate the properties of elastic formations, FWI has to take anisotropy into account. For example, Kamath and Tsvankin (2013, 2016) and Singh et al. (2018) develop efficient methodologies of elastic FWI for transversely isotropic media with a vertical symmetry axis (VTI). He et al. (2019) employ body and surface waves recorded on land to reconstruct the best-fit VTI model from elastic FWI. Li et al. (2018) utilize multicomponent reflection data to invert for the VTI parameters of a hydrocarbon reservoir. Liu and Tsvankin (2021) develop time-lapse elastic FWI for VTI media to monitor the temporal variations in the reservoir parameters.

Transverse isotropy with a tilted symmetry axis (TTI) provides a more accurate description of dipping TI layers or dipping fracture networks. For example, Singh et al. (2021b) show that FWI for TTI media yields more accurate estimates of the model parameters than previously used VTI algorithms. However, TTI models become inadequate for describing fractured sedimentary formations because systems of aligned fractures often create rocks with orthorhombic symmetry (Tsvankin, 1997; Tsvankin and Grechka, 2011).

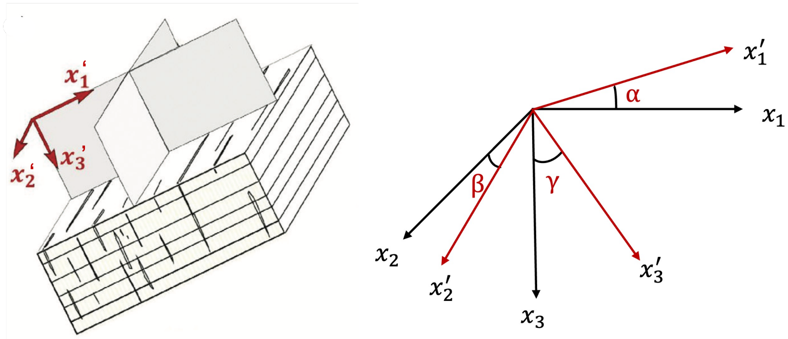

(a) (b)

Figure 1. (a) Tilted orthorhombic model with three orthogonal symmetry planes. (b) The orientation of the symmetry planes is defined using the Euler angles α, β, and γ (adapted from Liu and Tsvankin, 2019).

Zhou et al. (2015) reconstruct orthorhombic velocity models from wide-azimuth ocean-bottom cable data to improve imaging of fault structures. Wang and Tsvankin (2018) develop a computationally efficient methodology of acoustic FWI for 3D orthorhombic media. Maitra et al. (2018) obtain the P-wave orthorhombic velocity model by applying acoustic FWI and produce high-resolution migrated images of complex fault systems. Acoustic FWI for tilted orthorhombic media with the cross-correlation objective function is employed by Shao et al. (2020) to improve imaging of the Columbus basin in Trinidad. They demonstrate that incorporating orthorhombic symmetry helps resolve the heterogeneity in shallow gas layers. Singh et al. (2021a) incorporate lithologic constraints into FWI for orthorhombic media with a horizontal symmetry plane to reduce the nonlinearity of the inverse problem and increase the spatial resolution of the obtained parameters.

However, most existing applications of FWI to orthorhombic media are limited to models with a horizontal symmetry plane which are inadequate for many subsurface formations, such as dipping fractured layers. Here, we develop an elastic FWI algorithm for orthorhombic models with arbitrary orientation of the symmetry planes. The inversion is constrained using lithologic information that includes the P- and S-wave velocities and density obtained from well logs.

We begin with introducing the parameter definitions for tilted orthorhombic media. The workflow of multiscale elastic FWI, which includes finite-difference modeling for 3D orthorhombic media, is discussed next. The developed methodology is tested on a layered tilted orthorhombic model and on an orthorhombic version of the 3D SEG-EAGE overthrust model. To constrain the inversion, facies information obtained from well logs is incorporated into FWI using a convolutional neural network (CNN). Synthetic testing confirms that application of the lithologic constraints is critically important to reduce the nonuniqueness of FWI for low-symmetry anisotropic models.

2 THEORY

Orthorhombic models are characterized by three mutually orthogonal symmetry planes and can be defined using nine independent stiffness coefficients and the orientation of the symmetry planes (Tsvankin, 1997; Figure 1). If each symmetry plane coincides with a Cartesian coordinate plane, the stiffness matrix has the following form:

$$\mathbf{C} = \begin{pmatrix} C_{11} & C_{12} & C_{13} & 0 & 0 & 0 \\ C_{12} & C_{22} & C_{23} & 0 & 0 & 0 \\ C_{13} & C_{23} & C_{33} & 0 & 0 & 0 \\ 0 & 0 & 0 & C_{44} & 0 & 0 \\ 0 & 0 & 0 & 0 & C_{55} & 0 \\ 0 & 0 & 0 & 0 & 0 & C_{66} \end{pmatrix}. \tag{1}$$

The choice of notation is critical in multiparameter FWI because parameter tradeoffs may cause large inversion errors. Tsvankin (1997) shows that orthorhombic models can be conveniently described by the vertical P- and S-wave velocities and seven dimensionless Thomsen-style anisotropy coefficients. The performance of this and other parameterizations of orthorhombic media in anisotropic FWI is studied by Oh and Alkhalifah (2016) and Singh and Tsvankin (2022). Both papers study the radiation patterns of the model parameters, which provide information about the sensitivity of FWI to these parameters and the types of

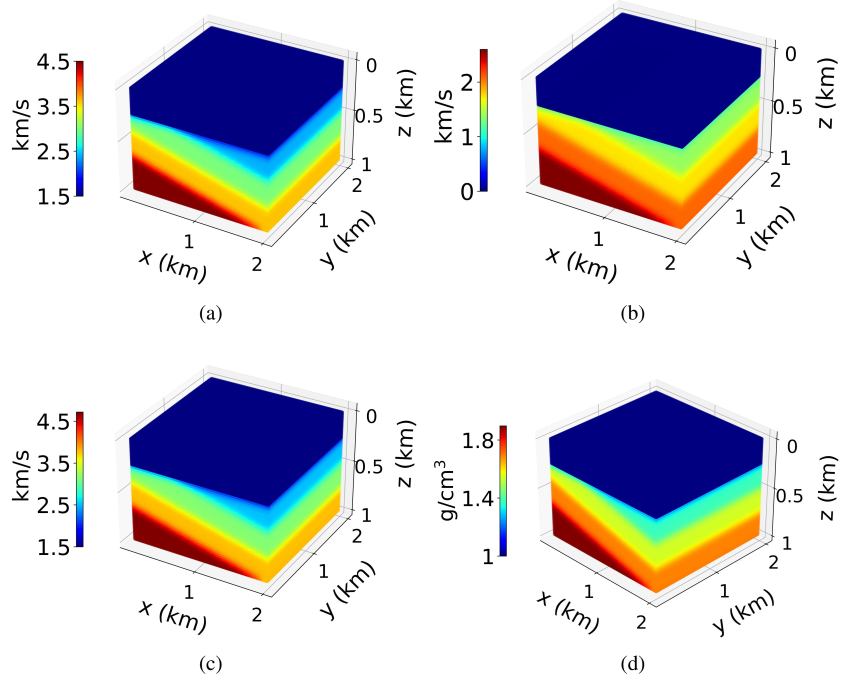

Figure 2. Parameters of a layered tilted orthorhombic model: (a) $\mathrm{V_{P0}}$, (b)$\mathrm{V_{S0}}$, (c) $\mathrm{V_{nmo,1}}$, and (d) ρ.

input data required for stable parameter estimation. The spatial resolution of the inverted parameters strongly depends upon the range of source-receiver offsets and azimuths of the acquired data. Singh et al. (2021a) and Singh and Tsvankin (2022) demonstrate that elastic FWI for orthorhombic media benefits from acquiring seismic data for large offset-to-depth ratios and a wide azimuthal range.

Singh and Tsvankin (2022) study the radiation patterns of the velocity-based parameters for orthorhombic models and discuss the advantages of that notation in parameter estimation (e.g., the velocity parameters have the same units and similar magnitudes). We use the velocity-based parameterization of Singh and Tsvankin (2022) supplemented by the Euler angles α, β, and γ that define the orientation of the symmetry planes. This parameterization consists of the P-wave ($\mathrm{V_{P0}}, \mathrm{V_{P1}}, \mathrm{V_{P2}}$) and the S-wave ($\mathrm{V_{S0}}, \mathrm{V_{S1}}, \mathrm{V_{S2}}$) velocities along the symmetry directions (i.e., the intersections of the symmetry planes), and the P-wave symmetry-plane normal-moveout (NMO) velocities ($\mathrm{V_{nmo,1}}, \mathrm{V_{nmo,2}}, \mathrm{V_{nmo,3}}$). The parameters $\mathrm{V_{nmo,1}}$ and $\mathrm{V_{nmo,2}}$ are the P-wave NMO velocities from horizontal reflectors in the $[x_2, x_3]$ and $[x_1, x_3]$-symmetry planes, respectively, for the unrotated model and $\mathrm{V_{nmo,3}}$ is the P-wave NMO velocity in the symmetry plane $[x_1, x_2]$. The Euler angles α and β describe the orientation of the normal to the symmetry plane $[x_1^{'}, x_2^{'}]$ and the angle γ defines the rotation of the other two symmetry planes.

The stiffness matrix D for a tilted orthorhombic medium is found using the Bond transformation:

$$\mathbf{D} = \mathbf{M} * \mathbf{C} * \mathbf{M}^{\mathrm{T}}, \tag{2}$$

where **C** is the stiffness matrix in the Cartesian coordinate system associated with the symmetry planes, **M** is the Bond transformation matrix (e.g., Winterstein, 1990), and $\mathbf{M}^{\mathrm{T}}$ is the transpose of **M**.

We assume that one of the symmetry planes of each orthorhombic layer coincides with the underlying reflector. This geologically plausible assumption has been often used for TTI models to reduce the nonuniqueness of the inverse problem (e.g., Liu and Tsvankin, 2019; Singh et al., 2021b). The orientation of that symmetry plane (reflector) can be obtained from migrated images and refined during the inversion which allows us to estimate the angles α and β. Therefore, only one Euler angle (γ) has to be obtained from FWI.

Wavefield propagation in tilted orthorhombic media is described by the elastic wave equation:

$$\rho \frac{\partial^2 u_i}{\partial t^2} = \frac{\partial}{\partial x_j} \left[D_{ijkl} \frac{\partial u_k}{\partial x_l} \right] + F_i, \tag{3}$$

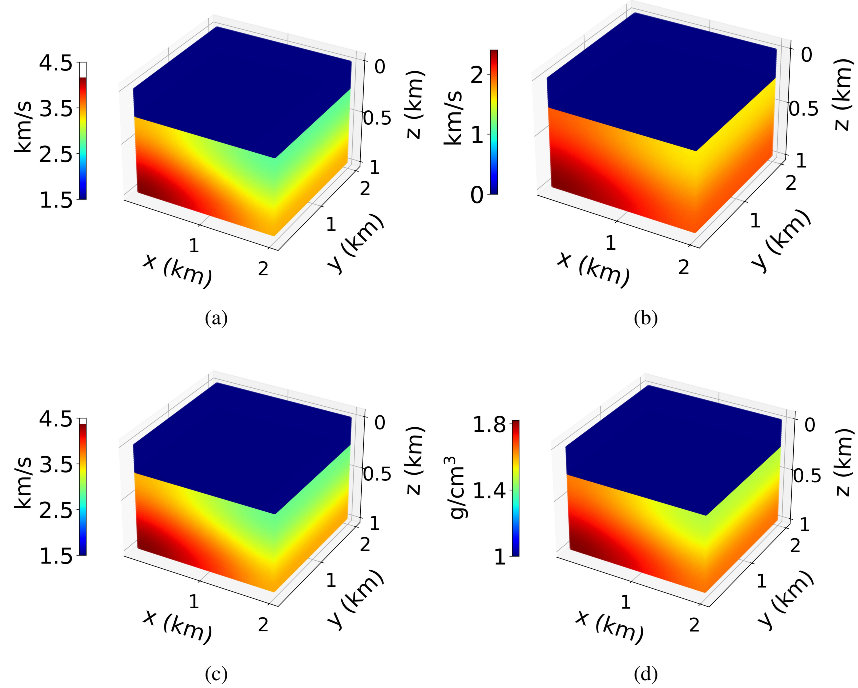

Figure 3. Several initial parameters of the model from Figure 2: (a) $\mathrm{V_{P0}}$, (b) $\mathrm{V_{S0}}$, (c) $\mathrm{V_{nmo,1}}$, and (d) ρ.

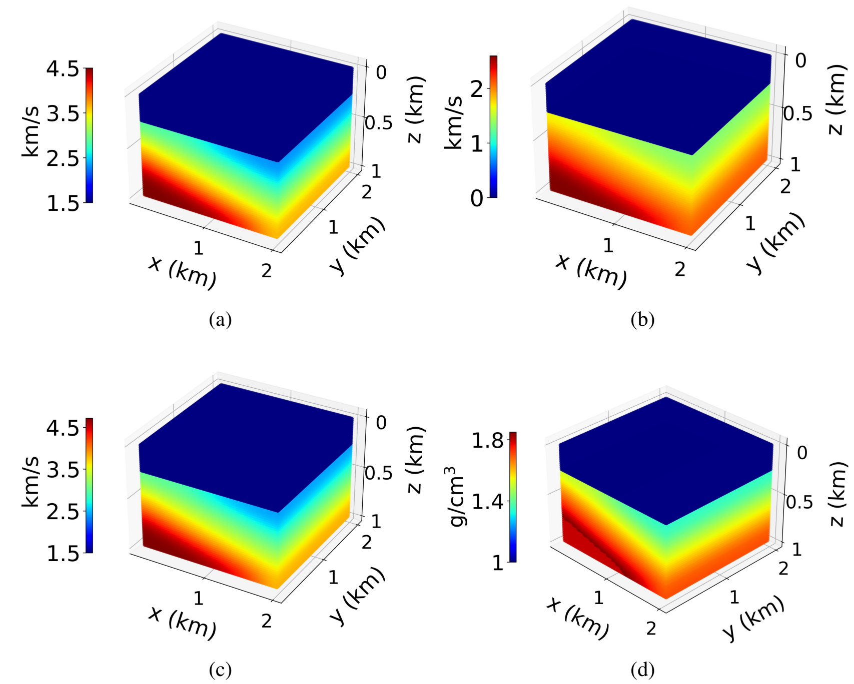

Figure 4. Inverted parameters for the model from Figure 2: (a) $\mathrm{V_{P0}}$, (b) $\mathrm{V_{S0}}$, (c) $\mathrm{V_{nmo,1}}$, and (d) ρ.

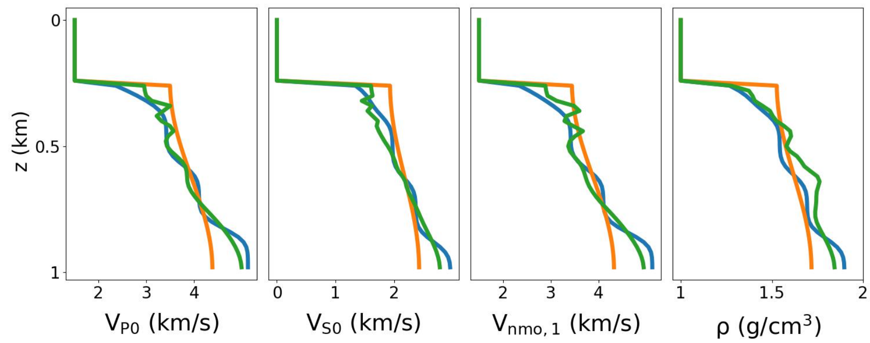

Figure 5. Vertical parameter profiles for the model from Figure 2 at $x = y = 1$ km. The actual parameters are marked by the blue lines, the initial parameters by the orange lines, and the inverted parameters by the green lines.

where **u** is the displacement vector, ρ is the density, **D** is the stiffness matrix defined in equation 2, and **F** is the body force per unit volume. Synthetic wavefields are computed by solving equation 3 using the finite-difference method of the fourth order in space and the second order in time. The misfit between the observed and simulated data is evaluated using the L_2-norm objective function:

$$E(\mathbf{m}) = \sum_{s=1}^{n_s} ||\mathbf{d}^{\mathrm{obs}} - \mathbf{d}^{\mathrm{sim}}(\mathbf{m})|| \tag{4}$$

where $\mathbf{d}^{\mathrm{obs}}$ is the observed data, $\mathbf{d}^{\mathrm{sim}}(\mathbf{m})$ is the data simulated for the model **m**, and n_s is the number of sources. The gradients of the objective function with respect to the model parameters are calculated with the adjoint-state method (e.g., Kamath and Tsvankin, 2016):

$$\frac{\partial E(\mathbf{m})}{\partial \mathbf{m}_n} = -\left(\frac{\partial D_{ijkl}}{\partial C_{pqrs}} * \frac{\partial C_{pqrs}}{\partial m_n}\right)\left(\int_0^T \frac{\partial u_i}{\partial x_j}\frac{\psi_k}{x_l}\ dt\right), \tag{5}$$

where the indices $i, j, k, l, p, q, r, s = 1, 2, 3$, T is the total time of wave propagation, and **u** and $\boldsymbol{\psi}$ are the forward and backward propagated displacement fields; summation over repeated indices is implied. According to equation 2, D_{ijkl} is the function of the stiffnesses C_{pqrs} in the coordinate system associated with the symmetry planes and the angles α, β, and γ. The model is updated using the conjugate-gradient method.

In the tests below, we use a multiscale FWI approach with four frequency bands (2-5 Hz, 2-8 Hz, 2-13 Hz, and 2-18 Hz). At the first stage, the observed and synthetic data are filtered for the frequency band 2-5 Hz. The inverted parameters are then used as the initial values for the next stage. The velocity-based parameters and density are updated at each iteration, whereas the rotation angle (γ) is updated only after the completion of each inversion stage.

3 SYNTHETIC TESTS

The developed FWI algorithm is tested on two 3D orthorhombic models with tilted symmetry planes. For the first, relatively simple model (Figure 2), we use 100 explosive sources at a depth of 40 m in the water column and record the wavefields by 2700 multicomponent receivers at the seafloor. The maximum offset is 1.8 km and the maximum offset-to-depth ratio for the bottom of the model is 1.4. As mentioned above, one of the symmetry planes in each layer is assumed to coincide with the underlying reflector, so the azimuthal and polar angles (α and β) of the normal to that plane are estimated from the migrated images. The initial model is generated by Gaussian smoothing (standard deviation = 15) of the actual parameters, and the initial rotation angle γ in each layer is set to zero. Figures 2, 3, and 4 display only four model parameters because all velocity fields have a similar structure.

As mention before, we employ the multiscale FWI approach, starting with low-frequency data and incorporating higher frequencies at the later inversion stages. The four frequency bands are 2-5 Hz, 2-8 Hz, 2-13 Hz, and 2-18 Hz. The inversion gradients are smoothed along the layers to suppress numerical artifacts.

The inverted parameters are significantly improved compared to their initial values. The P- and S-wave velocities along the symmetry directions are resolved better than the other parameters. The accuracy of the P-wave NMO velocities is generally acceptable, whereas the density is the least resolved parameter. There are some numerical artifacts generated during the inversion

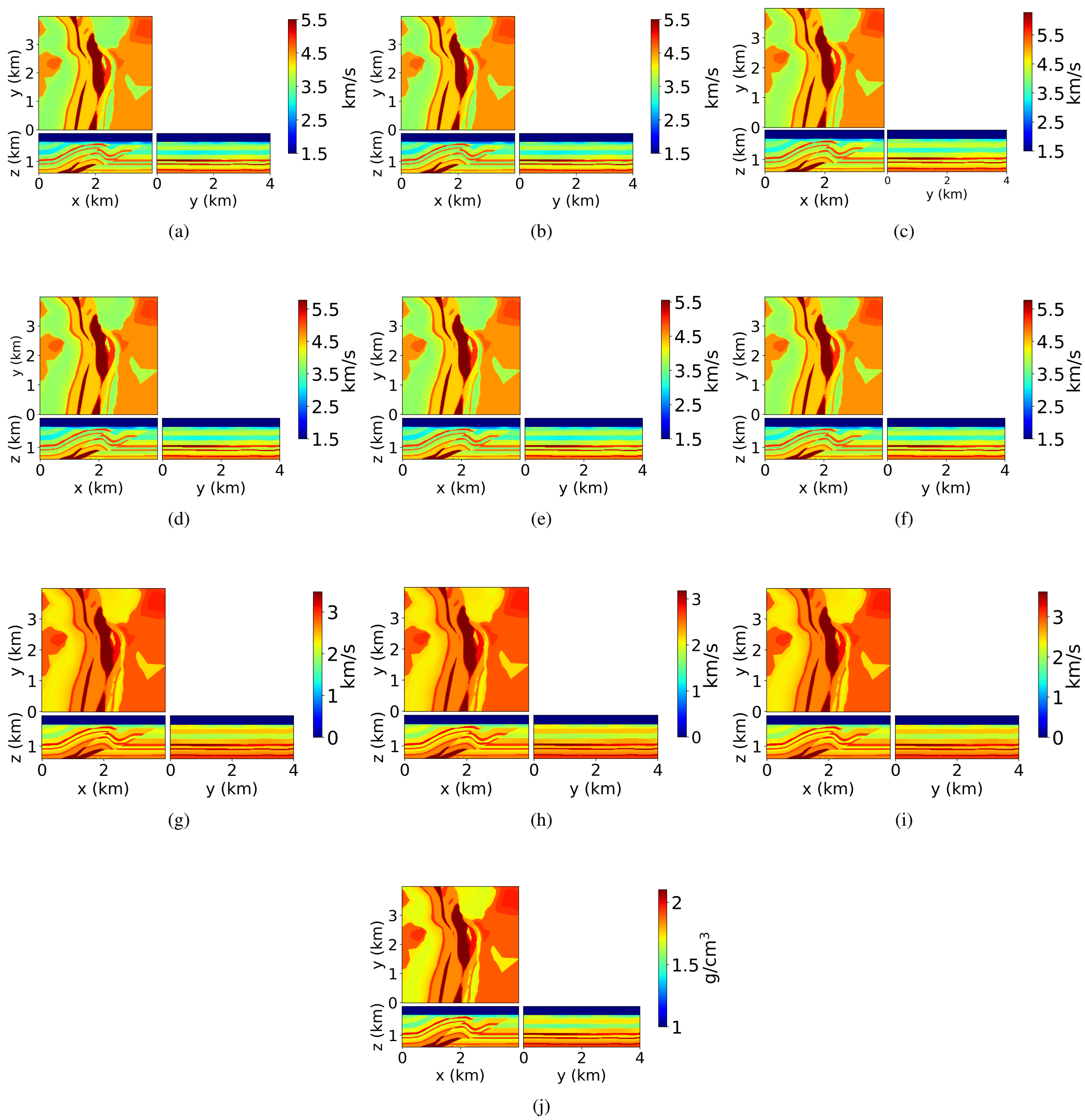

Figure 6. Parameters of the orthorhombic overthrust model: (a) V_{P0}, (b) V_{P1}, (c) V_{P2}, (d) $V_{nmo,1}$, (e) $V_{nmo,2}$, (f) $V_{nmo,3}$, (g) V_{S0}, (h) V_{S1}, (i) V_{S2}, and (j) ρ.

primarily because the objective function is multimodal. Taking the tilt of the symmetry plane into account helps properly constrain the spatial positions of the dipping reflectors.

Figure 5 shows the vertical profiles of the actual, initial, and inverted parameters at the center of the model. Although the actual model is not fully recovered, the improvements compared to the initial parameter values are clearly visible.

The second test is performed on an orthorhombic version of the 3D SEG-EAGE overthrust model (Singh et al., 2021a; Figure 6). The orientations of the orthorhombic symmetry planes are spatially variable. The wavefield is excited by 100 sources placed at 40 m below the water surface and recorded by 2700 receivers evenly distributed over the seafloor at a depth of 260 m to provide

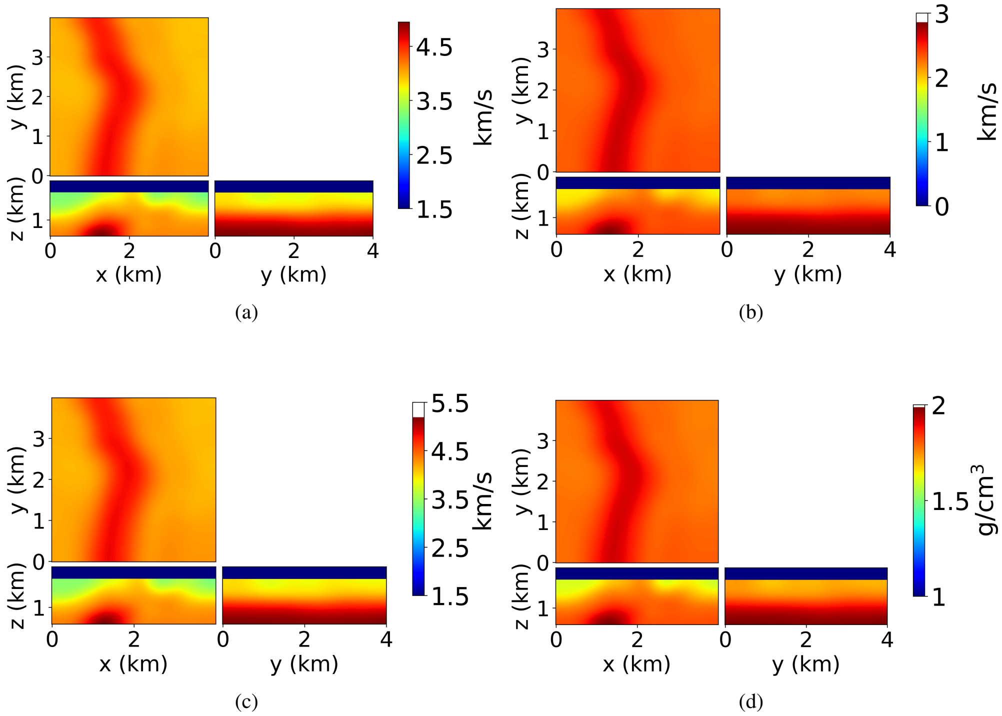

Figure 7. Initial parameters of the overthrust model: (a) $\mathrm{V_{P0}}$, (b)$\mathrm{V_{S0}}$, (c) $\mathrm{V_{nmo,1}}$, and (d) ρ.

wide azimuthal coverage. The maximum source-receiver offset is 3.6 km and maximum offset-to-depth ratio for the bottom of the model is about 2.6. The Ricker wavelet with a central frequency of 10 Hz is used as the source signal.

The initial parameters (Figure 7) are generated by Gaussian smoothing (standard deviation= 10) of the actual parameter fields; the initial value of the rotation angle (γ) is set to zero. We apply the multiscale FWI algorithm described above with the same frequency bands as in the first test. The inversion gradients are smoothed spatially at each iteration to suppress numerical artifacts. As before, the polar and azimuthal angles (α and β) of the normal to one of the symmetry planes are computed from the reflector orientations on the migrated images. The remaining Euler angle (γ) is estimated by FWI.

The P-wave symmetry-direction velocities are well-resolved, whereas the S-wave velocities are estimated with sufficient resolution only in the shallow layers (above 1 km; Figure 8). The P-wave NMO velocities and density are only partially resolved with marginal improvements compared to their initial values. The updates in these parameters are particularly small in the thin sedimentary layers, as can be observed on the vertical parameter profiles in Figure 13 below.

3.1 Lithologic constraints

To improve the accuracy and resolution of the inverted parameters, we incorporate lithologic constraints using a convolutional neural network (CNN). Lithologic facies classification from sonic and density well logs helps constrain the relationship between the elastic parameters and reservoir properties. Here, facies information is used only to build a more accurate initial model. Facies classification by a seismic interpreter is a time-consuming process that often leads to errors and involves significant uncertainties. Alternatively, facies classification can be performed by supervised machine-learning algorithms, such as support vector machines, gradient boosting classifiers, and random forest classifiers (Hall, 2016; Bestagini et al., 2017; Singh et al., 2021a). Here, we employ convolutional neural networks (CNNs) which represent one of the most effective machine-learning techniques for pattern-recognition and classification tasks.

The proposed CNN consists of the input layer, six hidden dense layers, and output layer. The input parameters (features) such as the P-wave vertical velocity, one of the S-wave vertical velocities (shear waves split into the fast and slow modes), density, and depth are used to train the network. The outputs (labels) are the rock facies (Figure 10). We use 10 boreholes that provide sonic

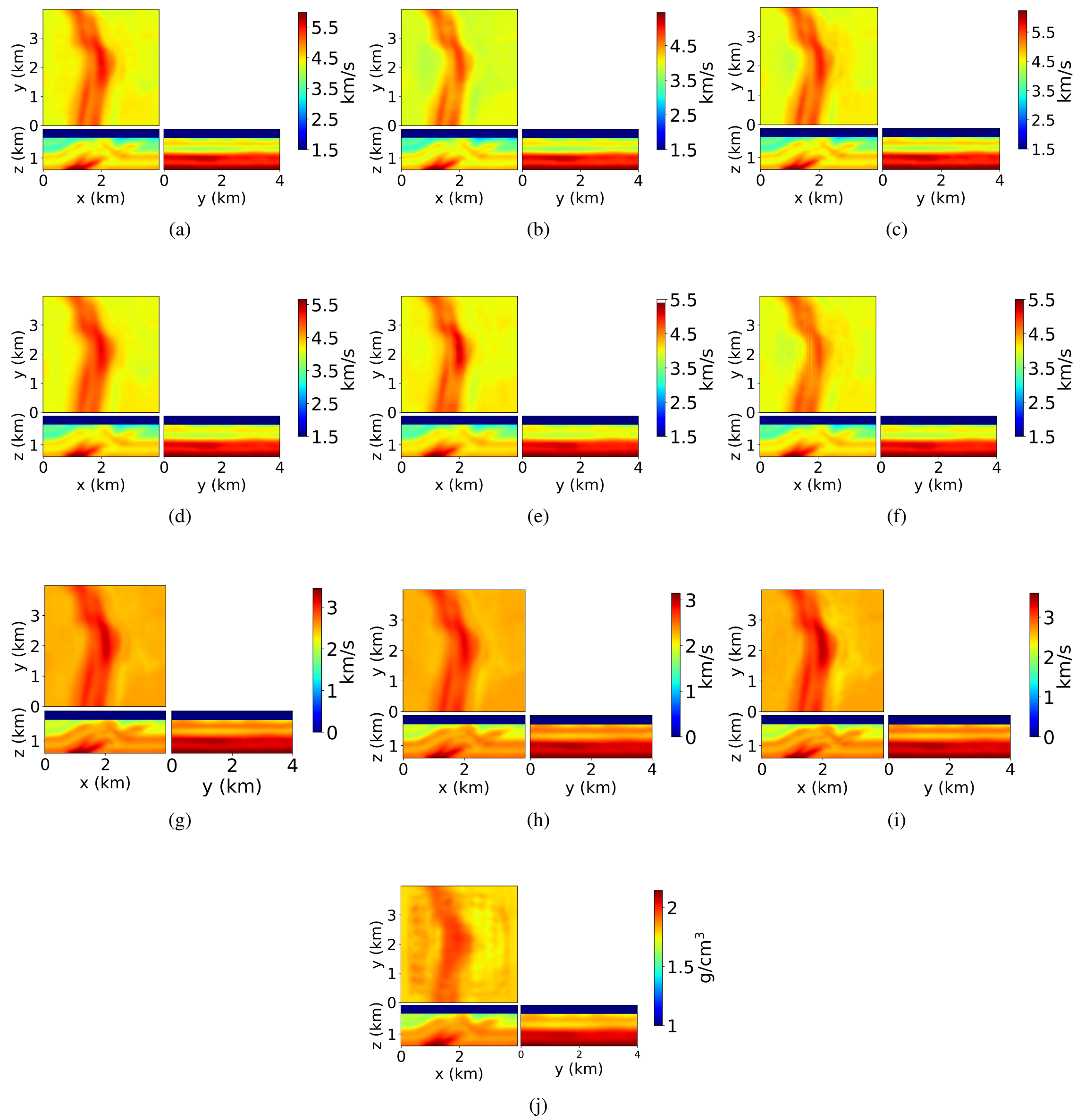

Figure 8. Parameters of the overthrust model estimated without using any constraints: (a) $\mathrm{V_{P0}}$, (b) $\mathrm{V_{P1}}$, (c) $\mathrm{V_{P2}}$, (d) $\mathrm{V_{nmo,1}}$, (e) $\mathrm{V_{nmo,2}}$, (f) $\mathrm{V_{nmo,3}}$, (g) $\mathrm{V_{S0}}$, (h) $\mathrm{V_{S1}}$, (i) $\mathrm{V_{S2}}$, and (j) ρ.

and density logs and the corresponding facies information. The CNN is trained on the well logs from eight boreholes, whereas the data from the two remaining boreholes are used for validation purposes. The prediction accuracy of the CNN on the training data is 99.2% and on the validation data 98.5%.

The trained CNN is then used to predict the facies information for the entire overthrust model from the inverted parameters ($\mathrm{V_{P0}}$, $\mathrm{V_{S0}}$, and ρ) estimated by the unconstrained FWI. It is assumed that the borehole data provide only the parameters $\mathrm{V_P}$, $\mathrm{V_S}$, and ρ that can be obtained from conventional sonic and density logs. We also calculate these model parameters from the available well logs using an interpolation technique. Then the initial parameters are estimated by the weighted averaging of the facies-generated and interpolated parameters. Finally, a Gaussian-based (standard deviation = 6) smoothing technique is applied to the parameters $\mathrm{V_{P0}}$, $\mathrm{V_{S0}}$, and ρ. The remaining parameters ($\mathrm{V_{P1}}$, $\mathrm{V_{P2}}$, $\mathrm{V_{S1}}$, $\mathrm{V_{S2}}$, $\mathrm{V_{nmo,1}}$, $\mathrm{V_{nmo,2}}$, and $\mathrm{V_{nmo,3}}$) have the same initial values as the ones previously used in the unconstrained inversion.

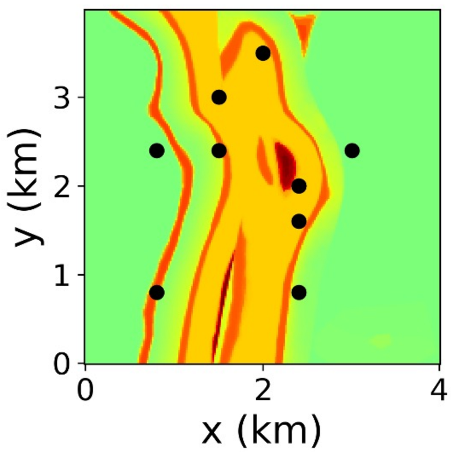

Figure 9. Horizontal cross-section of the velocity V_{P0} at z = 1.1 km showing the well locations marked by the black circles. The logs from these wells are used for facies classification.

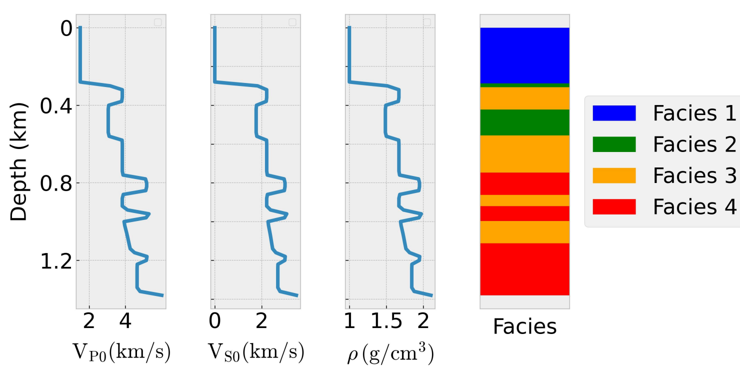

Figure 10. Facies classification using the sonic and density logs from the well located at $x = 1.8$ km and $y = 1.2$ km. Four facies are identified on the basis of the log properties.

The inclusion of the lithologic (facies) information produces an improved initial model and increases the accuracy and resolution of the inverted parameters, in particular of the vertical P- and S-wave velocities (V_{P0} and V_{S0}). There is also an improvement in density which is particularly significant in the thin sedimentary layers that are poorly resolved by the unconstrained FWI. The accuracy of the P-wave NMO velocities is also higher compared to the results of the unconstrained inversion despite some numerical artifacts. The vertical parameters profiles (Figure 13) clearly demonstrate the improvements achieved by incorporating the facies constraints into building the initial model for FWI.

4 CONCLUSIONS

We developed a 3D elastic FWI algorithm for tilted orthorhombic media and tested it on wide-azimuth multicomponent reflection data from two synthetic models. There are trade-offs between the inverted parameters due to the multimodal nature of the objective function for this low-symmetry anisotropic medium. In particular, the trade-offs reduce the accuracy of the S-wave symmetry direction velocities, P-wave NMO velocities, and density. Therefore, we incorporate lithologic information using convolutional neural networks to mitigate the influence of tradeoffs and increase the spatial resolution of FWI. The developed CNN generates a facies model from sparse borehole data, which is utilized to construct an improved initial model for FWI. The more accurate initial model helps suppress numerical artifacts and increase the accuracy of the inversion results. The results demonstrate that the developed elastic FWI algorithm is capable of recovering the parameters of tilted orthorhombic media with sufficient spatial

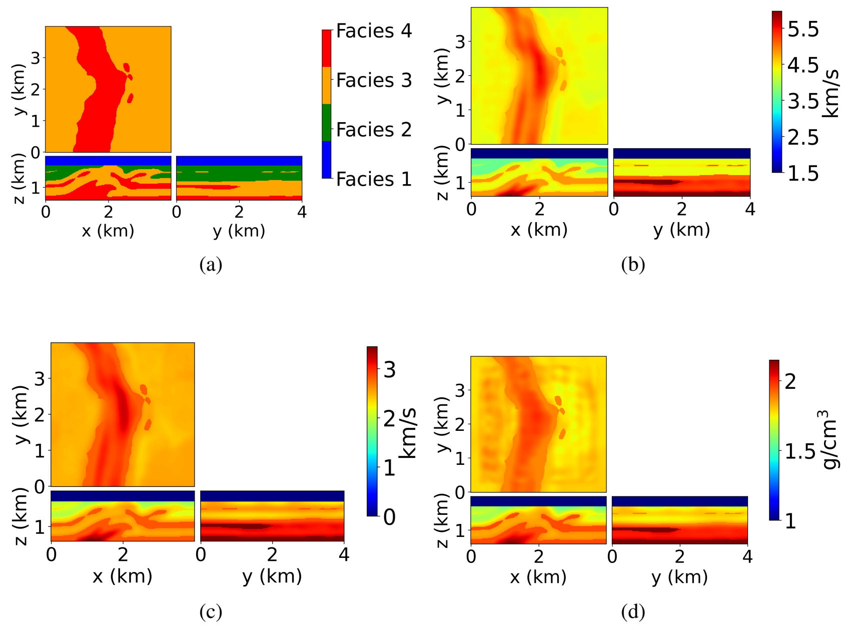

Figure 11. (a) Facies model generated by the developed CNN using the parameters estimated by the unconstrained FWI. Facies-constrained initial parameters: (b) V_{P0}, (c) V_{S0}, and (d) ρ.

resolution. The employed facies constraints make the method applicable to tilted orthorhombic media with significant structural complexity.

5 ACKNOWLEDGMENTS

This work is supported by the Consortium Project on Seismic Inverse Methods for Complex Structures at the Center for Wave Phenomena (CWP). We thank former CWP students Sagar Singh, Harpreet Sethi (both at NVIDIA), Yanhua Liu (Shell), and Werter Silva (Petrobras) for their useful suggestions and help in the code development.

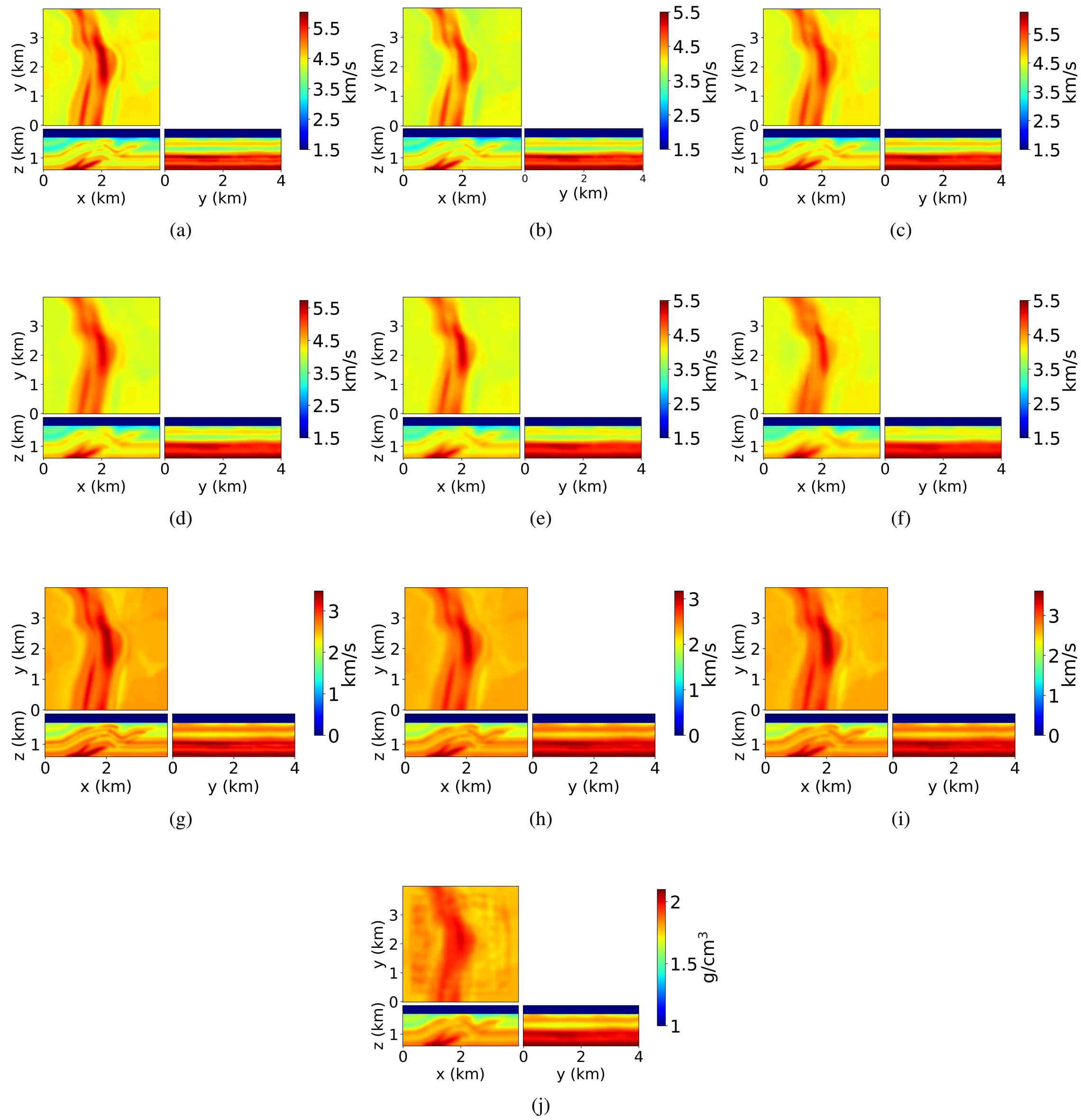

Figure 12. Inverted parameters obtained after including facies information: (a)$\mathrm{V_{P0}}$, (b) $\mathrm{V_{P1}}$, (c) $\mathrm{V_{P2}}$, (d) $\mathrm{V_{nmo,1}}$, (e) $\mathrm{V_{nmo,2}}$, (f) $\mathrm{V_{nmo,3}}$, (g) $\mathrm{V_{S0}}$, (h) $\mathrm{V_{S1}}$, (i) $\mathrm{V_{S2}}$, and (j) ρ.

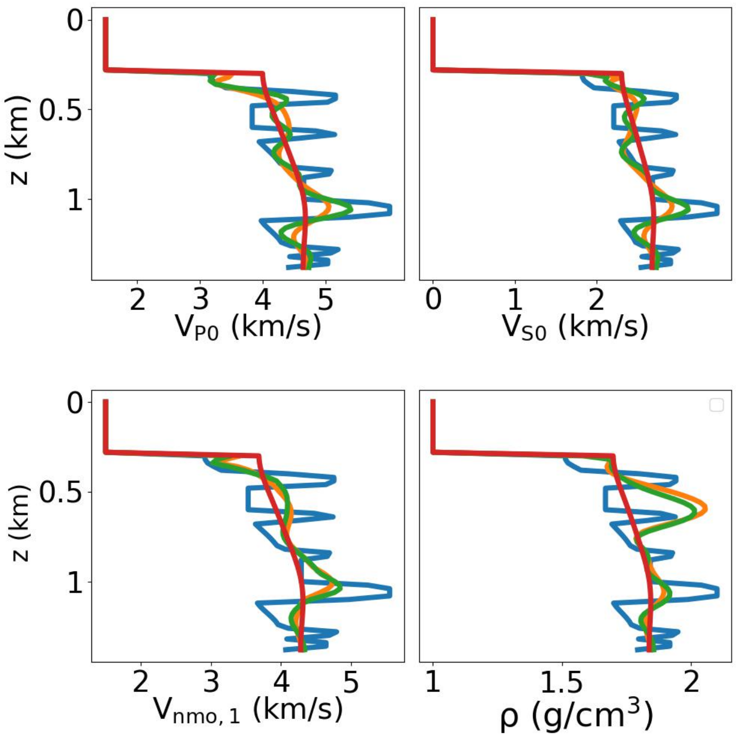

Figure 13. Vertical parameter profiles at $x = y = 1.6$ km. The actual parameters are marked by the blue lines, the initial parameters by the red lines, the parameters estimated by the unconstrained FWI by the orange lines, and the parameters estimated after including the lithologic constraints by the green lines.

6 APPENDIX A

7 FWI GRADIENTS FOR TILTED ORTHORHOMBIC MEDIUM

If the symmetry planes of the orthorhombic model coincide with the Cartesian coordinate planes, the stiffness coefficients in the two-index (Voigt) notation can be expressed in terms of the velocity-based parameters as follows (Singh et al., 2021a):

$$c_{11} = \rho\, V_{\rm P2}^2, \tag{A-1}$$

$$c_{22} = \rho\, V_{\rm P1}^2, \tag{A-2}$$

$$c_{33} = \rho\, V_{\rm P0}^2, \tag{A-3}$$

$$c_{12} = \rho\, \sqrt{\left(V_{\rm P2}^2 - V_{\rm S2}^2\right)\left(V_{\rm nmo,3}^2 - V_{\rm S2}^2\right)} - V_{\rm S2}^2, \tag{A-4}$$

$$c_{13} = \rho\, \sqrt{\left(V_{\rm P0}^2 - V_{\rm S0}^2\right)\left(V_{\rm nmo,3}^2 - V_{\rm S0}^2\right)} - V_{\rm S0}^2, \tag{A-5}$$

$$c_{23} = \rho\, \sqrt{\left(V_{\rm P0}^2 - V_{\rm S1}^2\right)\left(V_{\rm nmo,3}^2 - V_{\rm S1}^2\right)} - V_{\rm S1}^2, \tag{A-6}$$

$$c_{44} = \rho\, V_{\rm S1}^2, \tag{A-7}$$

$$c_{55} = \rho\, V_{\rm S0}^2, \tag{A-8}$$

$$c_{66} = \rho\, V_{\rm S2}^2. \tag{A-9}$$

The gradients of the objective function with respect to the velocity parameters m_n of the unrotated orthorhombic model are given in Singh et al. (2021a). If the symmetry planes are tilted, the inversion gradients can be found as (e.g., **?**):

$$\frac{\partial E(\mathbf{m})}{\partial m_n} = -\left(\frac{\partial D_{ijkl}}{\partial C_{pqrs}} * \frac{\partial C_{pqrs}}{\partial m_n}\right)\left(\int_0^T \frac{\partial u_i}{\partial x_j}\,\frac{\psi_k}{x_l}\;dt\right), \tag{A-10}$$

where the indices $i, j, k, l, p, q, r, s = 1, 2, 3$, T is the total time of wave propagation, and **u** and $\boldsymbol{\psi}$ are the forward- and backward-propagated displacement fields; summation over repeated indices is implied. Here, D_{ijkl} are the elements of the stiffness tensor of the tilted orthorhombic model, and C_{pqrs} are the stiffness tensor elements of the unrotated model with a horizontal symmetry plane (see equations 1 and 2).

The derivatives of the objective function with respect to the velocity parameters are:

$$\begin{aligned}\frac{\partial E}{\partial V_{\rm P0}} = -2\rho\, V_{\rm P0}\int_0^T \Bigg[&\left(\frac{\partial \psi_3}{\partial x_3}\frac{\partial u_1}{\partial x_1} + \frac{\partial \psi_1}{\partial x_1}\frac{\partial u_3}{\partial x_3}\right)\left(\sum_{ij}\frac{\partial d_{ij}}{\partial c_{13}}\right)\frac{f_2}{2} + \left(\frac{\partial \psi_2}{\partial x_2}\frac{\partial u_3}{x_3} + \right.\\ &\left.\frac{\partial \psi_3}{\partial x_3}\frac{\partial u_2}{\partial x_2}\right)\left(\sum_{ij}\frac{\partial d_{ij}}{\partial c_{23}}\right)\frac{f_3}{2} + \left(\frac{\partial \psi_3}{\partial x_3}\frac{\partial u_3}{\partial x_3}\right)\left(\sum_{ij}\frac{\partial d_{ij}}{\partial c_{33}}\right)\Bigg]\,dt,\end{aligned} \tag{A-11}$$

$$\frac{\partial E}{\partial V_{\rm P1}} = -2\rho\, V_{\rm P1}\int_0^T \left[\left(\frac{\partial \psi_2}{\partial x_2}\frac{\partial u_2}{\partial x_2}\right)\left(\sum_{ij}\frac{\partial d_{ij}}{\partial c_{22}}\right)\right] dt, \tag{A-12}$$

$$\begin{aligned}\frac{\partial E}{\partial V_{\rm P2}} = -2\rho\, V_{\rm P2}\int_0^T \Bigg[&\left(\frac{\partial \psi_1}{\partial x_1}\frac{\partial u_2}{\partial x_2} + \frac{\partial \psi_2}{\partial x_2}\frac{\partial u_1}{\partial x_1}\right)\left(\sum_{ij}\frac{\partial d_{ij}}{\partial c_{12}}\right)\frac{f_1}{2}\\ &+ \left(\frac{\partial \psi_1}{\partial x_1}\frac{\partial u_1}{\partial x_1}\right)\left(\sum_{ij}\frac{\partial d_{ij}}{\partial c_{11}}\right)\Bigg]\,dt,\end{aligned} \tag{A-13}$$

$$\frac{\partial E}{\partial V_{\rm nmo,1}} = -2\rho\, V_{\rm nmo,1}\int_0^T \left[\left(\frac{\partial \psi_2}{\partial x_2}\frac{\partial u_3}{\partial x_3} + \frac{\partial \psi_3}{\partial x_3}\frac{\partial u_2}{\partial x_2}\right)\left(\sum_{ij}\frac{\partial d_{ij}}{\partial c_{23}}\right)\frac{1}{f_3}\right] dt, \tag{A-14}$$

$$\frac{\partial E}{\partial V_{\rm nmo,2}} = -2\rho\, V_{\rm nmo,2} \int_0^T \left[\left(\frac{\partial \psi_3}{\partial x_3}\frac{\partial u_1}{\partial x_1} + \frac{\partial \psi_1}{\partial x_1}\frac{\partial u_3}{\partial x_3} \right) \left(\sum_{ij} \frac{\partial d_{ij}}{\partial c_{13}} \right) \frac{1}{f_2} \right] dt, \tag{A-15}$$

$$\frac{\partial E}{\partial V_{\rm nmo,3}} = -2\rho\, V_{\rm nmo,3} \int_0^T \left[\left(\frac{\partial \psi_2}{\partial x_2}\frac{\partial u_1}{\partial x_1} + \frac{\partial \psi_1}{\partial x_1}\frac{\partial u_2}{\partial x_2} \right) \left(\sum_{ij} \frac{\partial d_{ij}}{\partial c_{12}} \right) \frac{1}{f_1} \right] dt, \tag{A-16}$$

$$\begin{aligned} \frac{\partial E}{\partial V_{\rm S0}} = \rho\, V_{\rm S0} \int_0^T \Bigg[&\left(\frac{\partial \psi_3}{\partial x_3}\frac{\partial u_1}{\partial x_1} + \frac{\partial \psi_1}{\partial x_1}\frac{\partial u_3}{\partial x_3} \right) \left(\sum_{ij} \frac{\partial d_{ij}}{\partial c_{13}} \right) \left(f_2 + \frac{1}{f_2} + 2 \right) \\ &+2 \left(\frac{\partial \psi_1}{\partial x_3} + \frac{\partial \psi_3}{\partial x_1} \right) \left(\frac{\partial u_1}{\partial x_3} + \frac{\partial u_3}{\partial x_1} \right) \left(\sum_{ij} \frac{\partial d_{ij}}{\partial c_{55}} \right) \Bigg] dt, \end{aligned} \tag{A-17}$$

$$\begin{aligned} \frac{\partial E}{\partial V_{\rm S1}} = \rho\, V_{\rm S1} \int_0^T \Bigg[&\left(\frac{\partial \psi_3}{\partial x_3}\frac{\partial u_2}{\partial x_2} + \frac{\partial \psi_2}{\partial x_2}\frac{\partial u_3}{\partial x_3} \right) \left(\sum_{ij} \frac{\partial d_{ij}}{\partial c_{23}} \right) \left(f_3 + \frac{1}{f_3} + 2 \right) \\ &+2 \left(\frac{\partial \psi_2}{\partial x_3} + \frac{\partial \psi_3}{\partial x_2} \right) \left(\frac{\partial u_1}{\partial x_2} + \frac{\partial u_3}{\partial x_2} \right) \left(\sum_{ij} \frac{\partial d_{ij}}{\partial c_{44}} \right) \Bigg] dt, \end{aligned} \tag{A-18}$$

$$\begin{aligned} \frac{\partial E}{\partial V_{\rm S2}} = \rho\, V_{\rm S2} \int_0^T \Bigg[&\left(\frac{\partial \psi_2}{\partial x_2}\frac{\partial u_1}{\partial x_1} + \frac{\partial \psi_{x_1}}{\partial x_1}\frac{\partial u_2}{\partial x_2} \right) \left(\sum_{ij} \frac{\partial d_{ij}}{\partial c_{12}} \right) \left(f_1 + \frac{1}{f_1} + 2 \right) \\ &+2 \left(\frac{\partial \psi_1}{\partial x_2} + \frac{\partial u_2}{\partial x_1} \right) \left(\sum_{ij} \frac{\partial d_{ij}}{\partial c_{66}} \right) \Bigg] dt, \end{aligned} \tag{A-19}$$

where

$$f_1 = \sqrt{\frac{V_{\rm nmo,3}^2 - V_{\rm S2}^2}{V_{\rm P2}^2 - V_{\rm S2}^2}}, \tag{A-20}$$

$$f_2 = \sqrt{\frac{V_{\rm nmo,2}^2 - V_{\rm S0}^2}{V_{\rm P0}^2 - V_{\rm S0}^2}}, \tag{A-21}$$

$$f_3 = \sqrt{\frac{V_{\rm nmo,1}^2 - V_{S1}^2}{V_{\rm P1}^2 - V_{\rm S1}^2}}. \tag{A-22}$$

Here, d_{ij} are the stiffness coefficients of the tilted orthorhombic model in the two-index (Voigt) notation and $i, j = 1, 2, 3, 4, 5, 6$.

REFERENCES

Bestagini, P., V. Lipari, and S. Tubaro, 2017, A machine learning approach to facies classification using well logs: 87th annual international meeting, seg, expanded abstracts, 2137–2142, doi: 10.1190/segam2017-17729805.1: Presented at the , Abstract.

Brossier, R., S. Operto, and J. Virieux, 2015, Velocity model building from seismic reflection data by full-waveform inversion: Geophysical Prospecting, **63**, 354–367.

Hall, B., 2016, Facies classification using machine learning: The Leading Edge, **35**, 906–909.

He, W., R. Brossier, L. Métivier, and R. Plessix, 2019, Land seismic multi-parameter fwi in elastic vti media by simultaneously interpreting body waves and surface waves: 81st EAGE Conference and Exhibition 2019, European Association of Geoscientists & Engineers, 1–5.

Kamath, N., and I. Tsvankin, 2013, Full-waveform inversion of multicomponent data for horizontally layered vti media: Geophysics, **78**, WC113–WC121.

———, 2016, Elastic full-waveform inversion for vti media: Methodology and sensitivity analysis: Geophysics, **81**, C53–C68.

Li, J., K. A. Innanen, W. Pan, and G. Yu, 2018, Frequency domain elastic fwi for vti media: SEG International Exposition and Annual Meeting, SEG, SEG–2018.

Liu, Q., and I. Tsvankin, 2019, Stacking-velocity tomography for tilted orthorhombic media: Geophysics, **84**, C171–C180.

Liu, Y., and I. Tsvankin, 2021, Methodology of time-lapse elastic full-waveform inversion for vti media: Journal of Seismic Exploration, **30**, 257–270.

Maitra, S., F. F. Basir, M. L. Ghazali, A. R. Ghazali, S. M. Sapiai, N. E. Kady, and T. Konuk, 2018, Orthorhombic full-waveform inversion and model building for azimuthal anisotropy in the presence of gas bodies, *in* SEG Technical Program Expanded Abstracts 2018: Society of Exploration Geophysicists, 5123–5127.

Oh, J.-W., and T. Alkhalifah, 2016, Elastic orthorhombic anisotropic parameter inversion: An analysis of parameterization: Geophysics, **81**, C279–C293.

Shao, G., X. Zhao, Q. Tong, R. Huang, D. Baptiste, L. Jiang, and B. Nolte, 2020, Fwi-driven orthorhombic modeling with obs data for reservoir imaging offshore trinidad: SEG International Exposition and Annual Meeting, SEG, D041S070R006.

Singh, S., A. I. Kanli, and S. Mukhopadhyay, 2018, Full waveform inversion in time and frequency domain of velocity modeling in seismic imaging: Fwisimat a matlab code: Earth Sciences Research Journal, **22**, 291–300.

Singh, S., and I. Tsvankin, 2022, Sensitivity analysis of elastic full-waveform inversion for orthorhombic media: Journal of Seismic Exploration, **31**, 105–130.

Singh, S., I. Tsvankin, and E. Z. Naeini, 2021a, Elastic fwi for orthorhombic media with lithologic constraints applied via machine learning: Geophysics, **86**, R589–R602.

———, 2021b, Facies-based full-waveform inversion for anisotropic media: a north sea case study: Geophysical Prospecting, **69**, 1650–1663.

Tarantola, A., 1984, Inversion of seismic reflection data in the acoustic approximation: Geophysics, **49**, 1259–1266.

Tsvankin, I., 1997, Anisotropic parameters and p-wave velocity for orthorhombic media: Geophysics, **62**, 1292–1309.

Tsvankin, I., and V. Grechka, 2011, Seismology of azimuthally anisotropic media and seismic fracture characterization: Society of Exploration Geophysicists.

Wang, H., and I. Tsvankin, 2018, Methodology of waveform inversion for acoustic orthorhombic media (vol 27, pg 211, 2018): JOURNAL OF SEISMIC EXPLORATION, **27**, 403–403.

Winterstein, D., 1990, Velocity anisotropy terminology for geophysicsts: Geophysics, **55**, 1070–1088.

Xu, S., D. Wang, F. Chen, Y. Zhang, and G. Lambare, 2012, Full waveform inversion for reflected seismic data: 74th EAGE Conference and Exhibition incorporating EUROPEC 2012, European Association of Geoscientists & Engineers, cp–293.

Zhou, B., J. Zhou, L. Liu, F. C. Loh, J. Liu, Y. Xie, Z. Wang, and X. Pu, 2015, Orthorhombic velocity model building and imaging of luda field with waz obc data: SEG International Exposition and Annual Meeting, SEG, SEG–2015.